Materials & Design 234 (2023) 112369

Contents lists available at ScienceDirect

Materials & Design

journal homepage: www.elsevier.com/locate/matdes

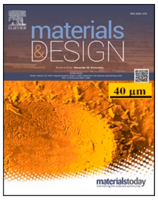

# Gradient structural anisotropy of dental enamel is optimized for enhanced mechanical behaviour

Máté Hegedűs [a], Viktória K. Kis [b,c,*], Ábel Szabó [a], Ivett Kovács [d], Noémi Rózsa [e], Zsolt Kovács [a,*]

[a] Department of Materials Physics, Eötvös Loránd University, H-1119 Budapest, Pázmány Péter sétány 1/a, Hungary
[b] Centre for Energy Research, Eötvös Loránd Research Network, H-1121 Budapest, Konkoly-Thege Miklós u. 29-33, Hungary
[c] Department of Mineralogy, Eötvös Loránd University, H-1119 Budapest, Pázmány Péter sétány 1/c, Hungary
[d] Institute for Geological and Geochemical Research, Research Centre for Astronomy and Earth Sciences, Eötvös Loránd Research Network, H-1112 Budapest, Budaörsi út 45, Hungary
[e] Semmelweis University, Faculty of Dentistry, Department of Pedodontics and Orthodontics, H-1088 Budapest, Szentkirályi u. 47, Hungary

## ARTICLE INFO

*Keywords:*
Primary dental enamel
Crystal orientation
Prism orientation
Gradient structure
Nanoindentation
Elastic modulus

## ABSTRACT

Exceptional mechanical performance of dental enamel in the harsh environment of oral cavity can be preserved on decade timescale, which is a unique property in comparison with functional nanomaterials. Hierarchic architecture of enamel, based on site-specific structural organization of apatite nanocrystals has a key role in this durability.

In the present study, a novel SEM imaging based method is presented for obtaining quantitative information on enamel prism orientation in sound primary dental enamel. This missing puzzle of quantification of the hierarchical enamel structure, along with spatial mechanical and chemical mapping, shed light on the optimum anisotropic gradient behaviour of elastic modulus of dental enamel.

Specifically, orientation and composition dependent contributions in both the spatially changing hardness and elastic modulus were separated. Anisotropy of the enamel's modulus was predicted and verified by the spatial variation of average prism orientation. Based on our results we conclude that the anisotropy of modulus for the bulk enamel arises from the elastic gradient in direction normal to the enamel external surface combined with the nearly constant value of modulus in the perpendicular cross section. This behaviour results in high surface strength and additionally can be responsible to the superior durability of human enamel.

## 1. Introduction

The structural organization of biological nanomaterials at multiple length scales provides notably higher bulk mechanical performance than that of the pure constituent material [1]. In human body, dental enamel is the hardest tissue, which exhibits high stiffness and toughness [2] together with good chemical resistance, and this combination of properties is unique in engineered materials. Moreover, the nanoscale dimensions of the building blocks of dental enamel allows a site specific tuning of their architecture [3] and crystal chemistry [4,5]. The so formed mesoscale structural gradients are intensely investigated and detailed descriptions of varying orientation distribution [3,6] and crystallographic parameters of the nanocrystals [6] are recently provided up to the millimetre length scale. However, we do not fully understand how this fine architecture formed by strictly regulated biological processes is optimized to control the bulk mechanical performance of dental enamel.

Dental enamel is composed of needle-shaped hydroxyapatite crystals of about 68x26 nm size in cross section [7] with length up to 10 μm [8]. The nanocrystals are ordered relative to their neighbours [3,9,10] and arranged into 80–130 nm thick fibrils, which are further organized into fibres with a diameter of 800 nm, which finally forms the enamel prisms of few micrometres of diameter [2]. The prisms are separated by interprismatic space [9,11]. The average orientation of hydroxyapatite nanocrystals depends on whether they are located inside the prism or in the interprismatic space [3,12]. Additionally, the arrangement of the prisms and the orientation of their long axis vary as function of distance from dentin-enamel junction (DEJ) creating strips or bundles called Hunter-Schreger bands. This organized architecture is a key factor in the effective mechanical response to stresses during mastication.

---

* Corresponding authors.
*E-mail addresses:* kis.viktoria@ek-cer.hu (V.K. Kis), kovacs.zsolt@ttk.elte.hu (Z. Kovács).

https://doi.org/10.1016/j.matdes.2023.112369
Received 31 January 2023; Received in revised form 12 September 2023; Accepted 25 September 2023

Experimental shear tests indicate that enamel prism orientation controls mechanical response over 5 % shear deformation [13]. According to multiscale numerical simulations, the arrangement of nanocrystals in the enamel prism contributes to an enhanced energy dissipation while stiffness and deformation resistance is preserved [14]. In addition, molecular dynamics simulations support the efficiency of crack deflection due to the organized misorientation of adjacent hydroxyapatite nanocrystals on micrometre scale [3].

The chemical composition of inorganic hydroxyapatite is $Ca_5(PO_4)_3OH$, while the crystal chemistry of biological hydroxyapatite of dental enamel exhibits substantial complexity. As a typical average composition, the $(Ca, Na, Mg, K, Sr)_5(PO_4,HPO_4,CO_3)_3(OH,F,Cl,CO_3)$ formula is used [15,16]. The concentration of minor components is not uniform over the whole volume of enamel. Gradual increase of Na and Mg concentration, together with the increase of the Ca/P ionic ratio and carbonate concentration towards the DEJ has been reported [17–21]. Besides this main trend, nanoscale graduation inside a single enamel nanocrystal is also revealed [22]. Variation of composition between anatomical sections of a single tooth [15], and also as function of tooth position in the dentition makes crystal chemistry of enamel hydroxyapatite a three dimensional function of position at multiple scales. As well as hierarchical architecture, concentration of trace elements was also found to affect mechanical properties. The increase of Na and Mg content in enamel cross section correlates with the decrease of hardness [20] while Mg incorporation into enamel surface by ion exchange experiments resulted increased hardness [23,24]. Similarly, experimentally increased surface Sr concentration of enamel contributes to prevent hardness loss under acidic conditions [25].

Organic content of mature enamel is about 0.1 w% [10]. By the end of amelogenesis, the proteins almost completely disappear from the mature enamel, but some organic residue remains in between the crystallites. The remained matrix protein accumulates within pores of 20–30 nm of diameter, which are distributed inhomogeneously in the interprismatic area, where crystallite orientation sharply changes [26]. The distribution of pores also exhibit spatial variation, gradually decreases from the DEJ towards the external enamel surface (EES) [27]. Protein content regulates mechanical properties of enamel [28], reduce hardness and elastic modulus [29] and affect flow properties of enamel by redistributing external stresses [30,31].

The continuously changing architecture and crystal chemistry results graded mechanical properties of dental enamel. The site dependent anisotropic mechanical response of human permanent enamel have been reported previously [20,21,30,32–37]. Based on their indentation tests, some authors argue that the anisotropy is related to the arrangement of nanocrystals and prism orientation [33,38] however others claim that mechanical response is rather affected by the chemical composition [20,21,36,37,39] and the impact of prism orientation is minimal [39]. Apparent gradation in crystallinity, texture and hardness has been investigated in a combined microindentation and synchrotron diffraction study [40]. Also, the role of increasing porosity towards the DEJ in the reduction of hardness and modulus has been emphasized [27].

In this paper, we report a systematic microstructural and nanoindentation mapping in distal-mesial cross section of primary dental enamel with the aim of establishing a quantitative relationship between mesoscale structural gradient and bulk mechanical response. By mapping the gradually changing anisotropy of the structure and quantifying prism orientation distribution, microstructural features are interpreted in terms of bulk performance. We provide a spatial analysis of nanohardness and elastic modulus data, which allows separation of the effect of structural anisotropy on the mechanical response from the effect of composition. These results contribute to the better understanding of the function of the heterogeneous graded structure of dental enamel. As intratooth variation of mechanical properties is an important issue when dental restorations are designed, a deep knowledge of the correlation between of locally changing architecture, chemical composition and mechanical performance in dental enamel will promote the development of more durable and effective graded functional nanomaterials for dental applications.

## 2. Materials and experimental methods

### 2.1. Materials and sample preparation

Sound human primary teeth were provided by volunteers. The research procedure was approved by the Ethics Committee of the Semmelweis University, Budapest (approval no. 84/2020). One sound mandibular molar was selected for detailed characterization, and an additional set of analysis is provided in the Supplementary Material (Appendix A). According to the World Dental Federation, the studied molar is represented by the notation of 85. The molar was embedded in diphase dentacryl resin (SpofaDental Inc., Czech Republic). Cutting was performed with an Accutom-100 cutting machine (Struers, Denmark) equipped with a diamond sawing disc. The molar was divided into two halves, with the cut surfaces lying perpendicular to the distal-mesial division line. The cut surfaces of each halves were then grinded using a motorized LaboPol-20 polishing and grinding machine (Struers, Denmark) with silicon carbide grinding discs (P1200, P2400, P4000) by 250 rpm. Polishing cloths were used for the final step with aluminium oxide suspension with decreasing grain size (1 μm, 0.3 μm). Between each step, the specimen was gently cleansed under running water.

For the comparison of bioapatite and inorganic mineral apatite, a hydroxyapatite single crystal was used from Badersdorf (Austria). The single crystal sample was investigated in two orientations, parallel to the (001) and (100) crystallographic planes. The native (001) and (100) facets of the single crystal were gently polished before measurement to remove overgrown crystals from the surface. The polishing procedure was performed in the same way as for the tooth sample.

### 2.2. Nanoindentation

The nanoindentation tests were performed by using an UMIS-2000 (Ultra MicroIndentation System). The maximum indentation load was 50 mN with an approximate constant rate of 1 mN $s^{-1}$. On the distal-mesial cross section, 300 imprints were made in each measurement area in an arrangement of 10x30 matrix with 50 μm distance between the neighbouring imprints. On the buccal side altogether 31 nanoindentation test were performed along a line with 50 μm distance between the measurement points. On the apatite single crystal 18 tests were performed on the (100) and 18 on the (001) crystallographic plane.

Vickers square-based diamond pyramid was applied for the hardness measurements. A nominal Poisson's ratio ($\nu$) of 0.27 was used for the calculation of elastic modulus. Oliver-Pharr method [41] was applied to analyse the data and calculate the Vickers hardness and elastic modulus values. The selection of the measurement matrix was preceded in each case by a thorough inspection of the surface produced by grinding and polishing in order to avoid fractures and surface irregularities.

### 2.3. Micro X-ray diffraction (μ-XRD)

The determination of crystallite orientation was carried out by a Rigaku D/Max Rapid II. The diffractometer is operated with CuKα X-ray radiation generated at 50 kV and 0.6 mA equipped with a 100 μm collimator. Accordingly, the analysed area was approximately 100 μm in diameter. In order to select the measurement area precisely, a built-in CCD camera was used. The detector system uses a curved imaging plate, which is placed on the inner surface of a cylinder that surrounds the $\varpi$-axis at the centre. This setup allows recording of 2D diffraction images over a wide $2\Theta$ range. Orientation of the sample was adjusted by a rotational specimen holder to allow the appearance of 002 diffraction peak of hydroxyapatite in Bragg-Brentano geometry. In this position the (001) planes, which are parallel to the sample surface, will be in diffraction condition. To do so, the normal vector of the sample surface was set to 16° away from the X-ray beam in the diffraction plane, i.e. in the common plane of the beam and the centre line of the imaging plate. Acquisition time for each measurement was set to 4 min. The diffraction image was recorded by 2DP Rigaku software. Intensity was integrated in a ± 5° range perpendicular to centre line of the imaging plate. Experimental data was compared with a calculated reference hydroxyapatite diffraction pattern (crystal structure data from ICSD Database #203027, https://icsd.fiz-karlsruhe.de) using the CrystalDiffract software. Intensity determination was done by peak fitting using Gaussian peak shape function in Originlab software.

### 2.4. Scanning electron microscopy

Imaging of enamel surfaces was performed by using an FEI Quanta 3D FEG dual beam electron microscope (Schottky-type electron gun with 20 kV acceleration voltage and 4–20 pA current). In order to make enamel prism more visible with clear edges in the scanning electron microscope (SEM), the surfaces were etched by hydrochloric acid (10 %) 3 times for 2 min. Selection of etching time was chosen based on [42]. To avoid the charging effect of the specimen surface either water vapour was emitted into the sample chamber (SEM images of Fig. 1) or thin amorphous carbon layer was deposited onto the sample surface (SEM images of Fig. 2). In the first case LVSED (low-vacuum secondary electron detector) was used for the detection of secondary electrons (SE), while in the second case high vacuum mode was used. As secondary electron emission is more intense at edges and tips than on flat regions, for the construction of prism orientation maps, high (4096x3773 pixels) resolution SE images were used. We note that surface etching was performed after mechanical testing, X-ray diffraction and energy dispersive spectroscopy measurement, so the incidental effect of acidic treatment on data obtained during these measurements can be excluded. For the determination of the chemical composition of the specimens, a Hitachi TM4000Plus SEM equipped with an Oxford AZtec One 30 mm$^2$ energy dispersive spectroscopy (EDS) SDD detector was used. Point analyses were performed along a line perpendicular to DEJ, the distance between measurement points were 50 μm, as in case of nanoindentation tests. The live time of EDS measurements was set to 30 s, which provided adequate signal-to noise ratio for quantification of trace elements as well. Quantification of the spectra was performed based on Cliff-Lorimer method using the k-factors implemented in the evaluation software of the spectrometer. The applied accelerating voltage and beam current were 15 kV and 2.4nA, respectively.

### 2.5. SEM image processing

Image processing was done using the ImageJ software [43]. To obtain orientation maps, raw SE images (Fig. A2a) were adjusted for brightness and contrast in case of need. The image was then subjected to thresholding with the aim of defining points of highest intensity for each prism (Fig. A2b). These points were used for segmentation (Fig. A2c), resulting closed irregular shape around each intensity maximum. These irregular shapes correspond to virtual prism areas, being typically elongated, if the long axis of the prisms lay in the image plane, and appearing isometric, when the long axis is close to the normal of the image plane. An ellipse was fitted to the virtual prism areas (Fig. A2d), by approximating enamel prism with a simplified cylindric shape. Prism orientation was characterized by two parameters: i) the in-plane azimuthal angle of the main axis of the ellipse, which varies between 0 and 180° and ii) an out-of-plane inclination angle, which varies between 0 and 90° and can be estimated from the aspect ratio (AR) of ellipse's major and minor axes as arcsin(1/AR). For the orientation extremes, $AR = 1$ for 90° and $AR = \infty$ for 0° and indicated by blue and red colours (see diagrams Fig. 2e and f), respectively.

## 3. Results

### 3.1. Arrangement of enamel prisms

Fig. 1a-1b show the optical micrograph of the molar sample in different sections, indicating the areas selected for nanoindentation and EDS measurements (measurement areas 1–5). Prismatic structure was imaged by SEM using different magnifications (Fig. 1c-d). On the buccal surface (Fig. 1c), the enamel prisms are parallel to the electron beam of the SEM, so the keyhole-shaped cross section of the prisms is visible. The SEM images also show that all prisms are surrounded by an approximately 1 μm wide interprismatic area (Fig. 1c white arrow), the orientation of the hydroxyapatite crystallites differs from the orientation characteristic inside the enamel prism [3]. Fig. 1b shows the cut and polished distal-mesial cross-section of the molar near to the occlusal side. Prisms in this cross-section are aligned roughly perpendicular to the electron beam (Fig. 1d). However, in the low magnification part of Fig. 1d variation of prism orientation can be recognized as well. Additionally, aprismatic enamel at the buccal side was observed in ~20 μm thickness as well, which is in agreement with the range of 16–45 μm published by [44]. This layer was missing at the occlusal side of the tooth.

Prism orientation distribution has been analysed in SEM images (Fig. 2a and b) taken from etched surfaces at measurement areas 3 and 5, by image analysis procedure. Dissolution rate is different in prism and interprism areas and thus etching selectively enhances prism boundaries, which can be imaged using secondary electrons in the SEM. This pattern can be used to approximate prism structure. The surface section of each prism was fitted using an ellipse and the AR and the in-plane azimuthal angle of the major axis were used to characterize the local prism orientation. Based on minor axis lengths, average prism diameter proved to be 5.39 ± 1.59 μm and 4.30 ± 1.00 μm for measurement areas 3 (mesial side) and 5 (occlusal side), respectively (Fig. 2e and 2f), which is in agreement with the average value of 5 μm usually cited in literature [10,45]. From the AR the out-of-plane inclination angle of the prisms can be calculated and the two angles determine the three-dimensional orientation of the prisms with respect to the image plane. From the fitted data, coloured orientation maps were constructed (Fig. 2c and d). The probability distribution of prism orientation characteristic of the whole area of the SEM images is plotted on Fig. 2e and f. In measurement area 3 (mesial side) the aspect ratio of the prims falls into narrow range, which implies that the prisms mostly lay in the image plane (Fig. 2e). This is particularly true near to the EES, where the prism orientation is mostly homogeneous as seen in Fig. 2c. The inclination angle of the prisms scatters around 27° depending on the exact location in the imaged area. Both aspect ratio and inclination angle exhibit larger variation close to the DEJ, which is related to the Hunter-Schreger bands in this area (Fig. 2a and c).

On the occlusal side (measurement area 5) the aspect ratio of the prisms varies in a wider range (Fig. 2f) and their inclination angle spans for the whole 0–180° range. A minor preference around 90° can be observed, which indicates that the average prism orientation tends to be perpendicular to the EES, exhibiting however, significant dispersion. The large number of green coloured prisms on Fig. 2d indicates the presence of keyhole pattern seen in the distal-mesial cross section SEM image (Fig. 2b). In this case, the prisms are perpendicular to the cross section, which means that they lay approximately in the plane of the EES.

### 3.2. Nanoindentation measurements and chemical composition analysis of enamel

Nanoindentation measurements were carried out on flat polished surfaces of both the distal-mesial cross-section and the buccal side of the molar. The essential difference between the two surfaces prepared for nanoindentation is the elongation direction of the enamel prisms with

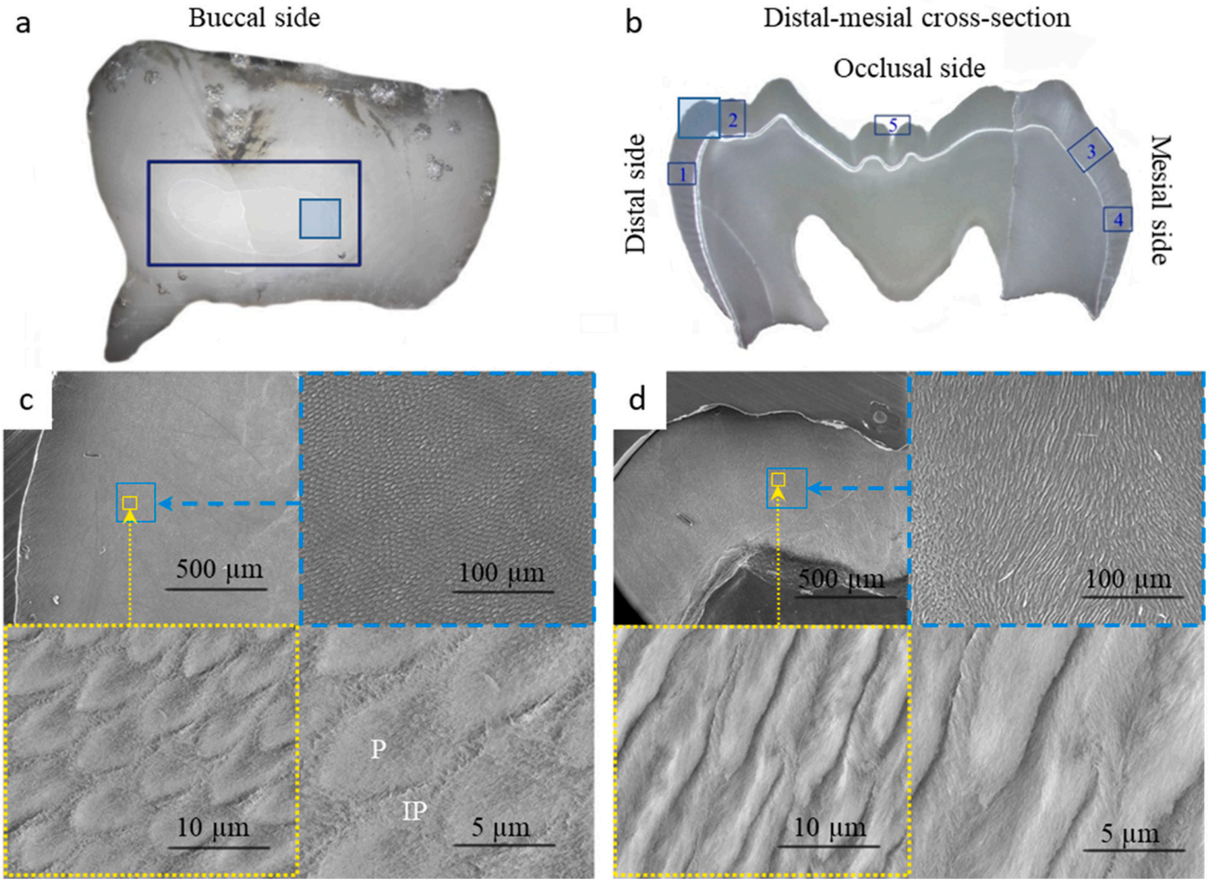

**Fig. 1.** Optical micrograph of the buccal surface (a) and distal-mesial cross section (b) of studied molar sample. Areas selected for nanoindentation and EDS measurements are indicated by numbers 1–5. Secondary electron SEM images of the enamel prism arrangement in different magnifications along the buccal surface (c) and in the distal-mesial cross-section near to occlusal side (d). Enlarged areas on (c and d) are indicated by shadowed boxes on (a and b). Prism (P) and interprism (IP) areas are indicated.

respect to the polished surface. Areas of nanoindentation measurement on the distal-mesial cross-section are shown in Fig. 1b. Vickers hardness (HV) and elastic modulus (E*) values for each nanoindentation test are shown in the maps in Fig. 3a and b, respectively. (Hereafter the notation of E* is used for the elastic modulus determined from the nanoindentation measurements to distinguished it from Young's modulus).

Additionally, Fig. 3c shows the corresponding map of nanohardness normalized with elastic modulus (HV/E*), which carries information on defect density [46] and allows the comparison of areas with different elastic modulus. According to Fig. 3a and b, the HV and E* values exhibit notable scatter at the same distance from the DEJ, however, the HV/E* typically decreases gradually from the surface towards the DEJ. At the same time, at the mesial side close to the tooth neck (measurement area 4) local hardening can be observed near to the EES. Namely, in this particular case the hardness distribution starts with a slight ascending zone (4.60 GPa) until it reaches the hardest zone (5.38 GPa) around 300 µm from the surface of the enamel, then continuously decrease towards the DEJ (4.07 GPa).

To visualize better the variation of the mechanical parameters (HV, E* and HV/E*) as function of distance from the EES, the values measured at the same distance were averaged and plotted in Fig. 4a–c. Elastic modulus values do not show the same decreasing tendencies as hardness through the entire thickness of the enamel (Fig. 4b). Difference between hardness and modulus curves originates from the fact that while the elastic modulus is about the average of the moduli of the structural components under the indenter, the hardness overestimates the effect of the mechanically softer volumes with structural defects. Modulus normalized hardness maps (Fig. 3b) seem to be more homogeneous, and a slight decreasing trend towards the DEJ can be observed on the averaged plots (Fig. 4b).

For comparison, the mechanical parameters measured on the buccal side are indicated by coloured bands in Fig. 4a-b as well, where the middle line of the bands represents the average values and the width of the bands corresponds to the standard deviation of the measurements. The average hardness and elastic modulus obtained on the buccal side were $HV_{buccal} = 6.17 \pm 0.5$ GPa and $E^*_{buccal} = 142 \pm 17$ GPa, respectively (Fig. 4a-b). For these measurements, the indentation direction was roughly parallel to the elongation direction of the enamel prisms observed on SEM images (Fig. 1c). (We note that producing suitable surface for SEM imaging requires the removal of up to 100 µm thick material, which may introduce some uncertainty when correlating prism arrangement with nanoindentation data). The average nanoindentation imprint size is of about 4 µm, which implies that all hardness values indicate an average of both interprismatic and prismatic regions. The HV and E* values measured on the distal-mesial cross section in measurement areas 1–4 are lower than the corresponding values on the buccal side, however, in case of measurement area 5, the HV values practically fall in the same band as the values measured on the buccal side (Fig. 4a). Similarly to buccal data, average hardness ($HV_{surface} = 5.2$ GPa) and modulus ($E^*_{surface} = 108.7$ GPa) can be obtained for the outer 100 µm thick zone of the distal mesial cross section (measurement areas 1–4), which allows the comparison of the mechanical properties of this zone in two perpendicular directions.

Chemical composition was determined by EDS on each nanoindentation measurement area as function of distance from the EES. Main (Ca and P) and minor (Na, Mg, Cl, Sr) components were plotted

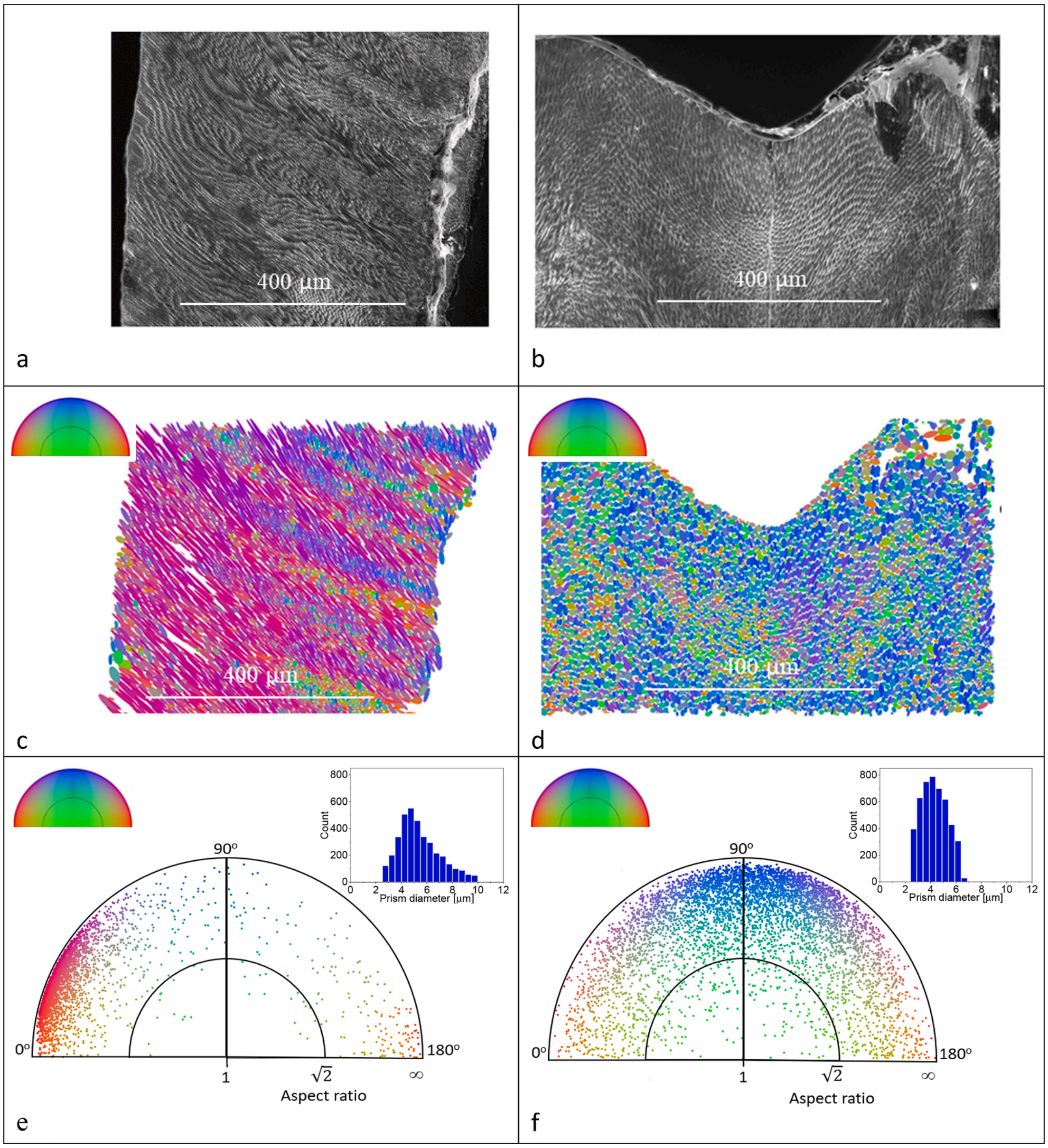

**Fig. 2.** Secondary electron SEM images of etched surfaces (a, b) and enamel prism orientation maps obtained by ellipse fitting of measurement areas 3 (c) and 5 (d). The colours represent aspect ratio and azimuthal inclination of prisms in the image plane. Two dimensional probability distribution diagram of prism orientations on measurement areas 3 and 5, are provided in (e) and (f), respectively. Prism diameter is approximated as the length of the minor axis, and frequency distribution of prism diameter in the two analysed areas is plotted in the right upper corner of (e) and (f). Colour code for prism orientation is provided in the upper left corner of (c-f).

separately to make tendencies more visible. Ca and P concentrations exhibit constant values through the whole cross section (Fig. 4d), however, on the mesial side close to the tooth neck area, these two main components decrease from the surface to the DEJ (Fig. 4d, measurement area 4). Regarding the concentration variation of minor elements, no difference is observable among the measurement sites. Na increases strongly, Mg increases slightly towards dentin, while Cl firmly decreases from the surface of the enamel and Sr shows constant value through the enamel (Fig. 4e).

In general, Ca/P ratio is a useful parameter to distinguish between calcium-phosphate phases and biogenic and inorganic apatites. For inorganic mineral apatite, ionic ratio equals 1.67. Minor elements such as Na, Mg and Sr can easily incorporate into the crystal lattice into the Ca position, therefore the ionic ratio was calculated according to the (Ca + Na + Mg + Sr)/P formula. Ionic ratio values of the measurement areas are plotted in Fig. 4f. Ionic ratio values in general are higher than the average value published for mature enamel (1.58, [15]), however, fall in the wide range of scatter (1.5–1.9, [47]). The higher values are due to an elevated amount of Ca, which is measured uniformly through the whole cross section. However, the change of ionic ratio (or Ca/P) as function of distance from the DEJ shows similar tendency as reported in other studies [20]. Measurement sites 1, 2, 4 and 5 show slight increase of ionic ratio from the surface of the enamel towards the dentin, while site 3 rather indicates constant tendency. The slight increase is probably related to the increasing carbonate content towards the DEJ [17–21].

### 3.3. Nanoindentation measurements on hydroxyapatite single crystal

For comparison to the nanostructured hydroxyapatite of enamel, measurements were performed on a hydroxyapatite single crystal as well. Hydroxyapatite crystallizes in hexagonal symmetry and, accordingly, exhibits anisotropy of physical properties (for details on the

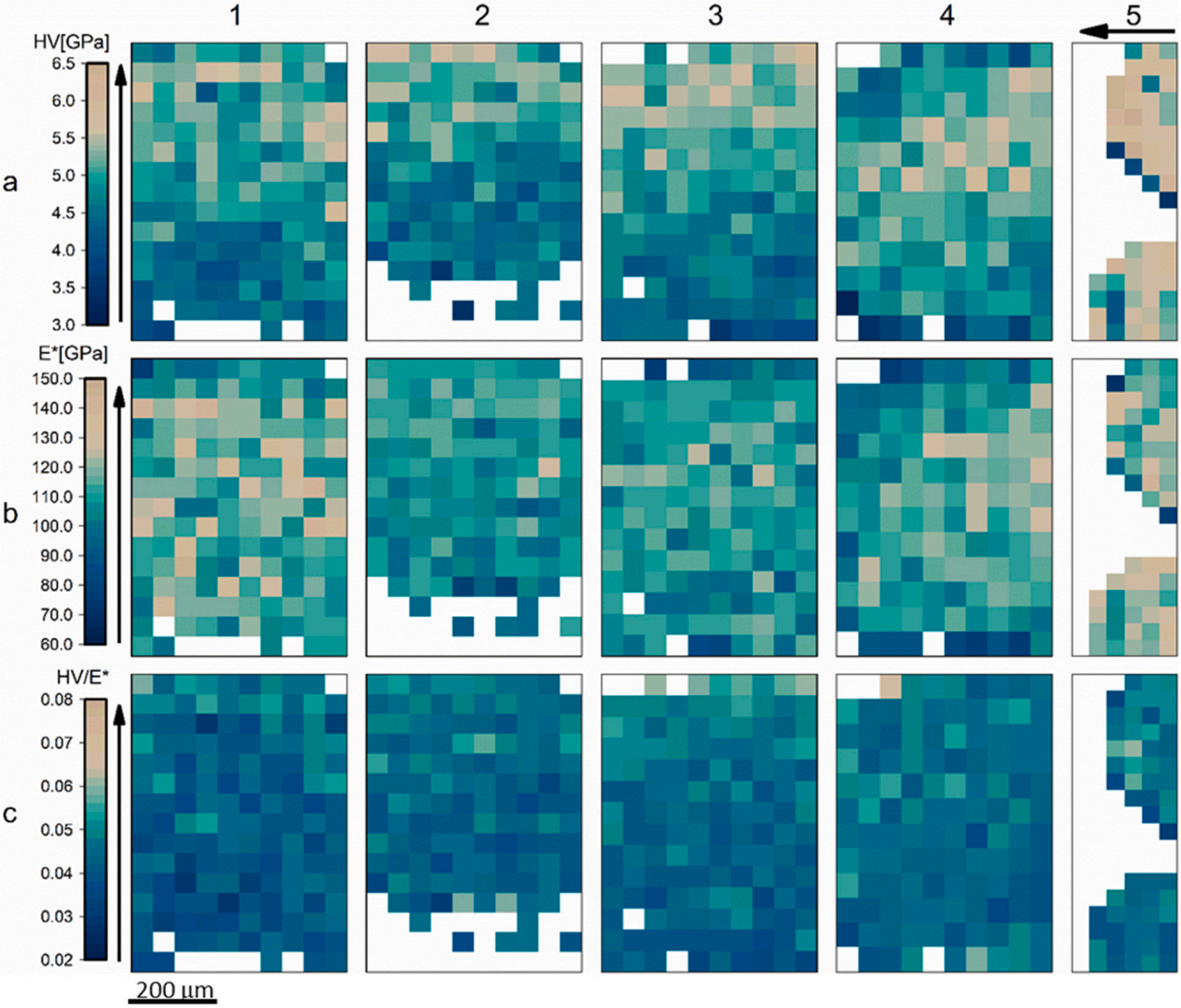

**Fig. 3.** Hardness (a), elastic modulus (b) and hardness/elastic modulus ratio (c) maps for the measurement areas on the distal-mesial cross-section. Column numbers 1–5 represent measurement areas indicated on Fig. 1. Blank pixels close to boundaries between enamel/glue, and enamel/dentin indicate uncertain values, which might not originate from enamel. Head of the arrows are pointing to the direction of the surface of the enamel. Pixel size is 50 × 50 µm$^2$.

anisotropic elastic parameters see Appendix C). The aim was to determine the average hardness along different crystallographic directions, namely on the (100) plane (perpendicular to the crystallographic **a** axis) and on the (001) basal plane (perpendicular to the crystallographic **c** axis) (Fig. 5).

According to our expectations, hydroxyapatite single crystal exhibits anisotropic mechanical response with a significantly lower average HV when the indentation direction is perpendicular to the (100) plane ($HV_a = 8.9 \pm 1.1$ GPa), with respect to the average HV measured on the (001) plane ($HV_c$ 10.5 ± 1 GPa). According to literature data, the nanohardness values obtained with indentation direction parallel to the [001] axis are 11 % higher than in the perpendicular direction [48], while in the present work the difference between the two average HV values was 18 %. Elastic modulus also shows orientation dependence, it is lower when the indentation direction is perpendicular to the (100) plane ($E_a$*=169 ± 3 GPa) and higher on the (001) plane ($E_c$* 197 ± 2 GPa). At the same time, modulus normalized nanohardness proved to be very similar in the two orientations.

### 3.4. Crystal orientation in enamel

Average orientation of the hydroxyapatite nanocrystals on the buccal side and in the distal-mesial cross section (near to the EES) was assessed by comparing diffraction peak intensities measured with µ-XRD to random orientation distribution (Fig. 6a).

In order to quantify the average orientation of the nanocrystals, intensity ratios were calculated using the $R_{hkl}$ texture index proposed by [40],

$$R_{hkl} = [I_{hkl}/I_{112}]/K_{hkl}, \tag{1}$$

where $K_{hkl}$ is the intensity ratio of the *hkl* to the 112 reflections of the random hydroxyapatite powder. $I_{hkl}$ is the measured intensity of the *hkl* reflection of bioapatite. In case of random orientation, $R_{hkl}$ equals to 1, while at $R_{hkl} > 1$, preferred *hkl* crystallite orientation is detected. Due to the difference between measurement geometry of the µ-XRD instrument and the ideal Bragg-Brentano condition, the quantitative data of texture index ($R_{hkl}$) have to be considered with concern. However, based on the intensity ratios of 002, and 030 reflections (Fig. 6a and also see Table B1 in Appendix B) we can claim that the average preferred orientation of bioapatite nanocrystals in the two sections is essentially different.

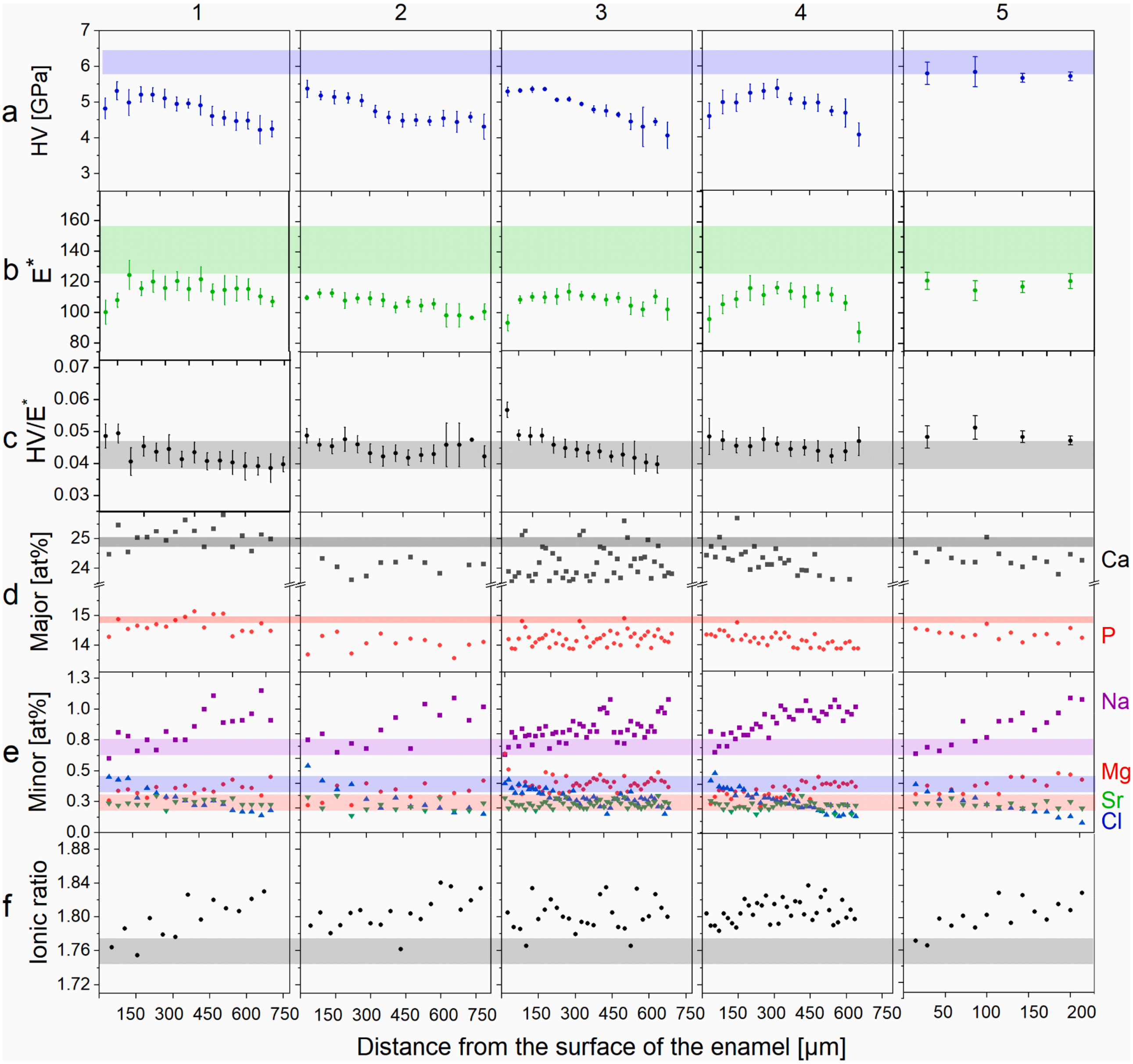

**Fig. 4.** Average hardness, HV (a), elastic modulus, E* (b) and HV/E* values (c) are plotted as a function of distance from the EES. The solid dots represent the average of 10 measurements performed at the same distance from the EES and the sticks represent the range of measured values at each distance. Major (d) and minor (e) chemical element composition determined by EDS-SEM as a function of distance from the EES. Ionic ratio values calculated according to (Ca + Mg + Na + Sr)/P formula (f). Coloured bands show the corresponding average value and the standard deviation of the buccal side measurements. Columns 1–5 represent measurement areas 1–5, respectively.

By plotting the $R_{hkl}$ values as function of the $\psi$ angle between the normal of the (*hkl*) planes and the **c** axis (Fig. 6b), further details on the orientation arrangement of the hydroxyapatite nanocrystals is revealed. On the buccal side, crystal planes with $\psi < 30^\circ$ have significantly larger intensities with respect to random orientation (i.e. $R_{hkl} > 1$), while planes with $\psi > 60^\circ$ show very small intensities with respect to random orientation (i.e. $R_{hkl}$ is close to zero). On contrary, in the distal-mesial cross section near to the EES, all crystal planes with $\psi > 60^\circ$ have extreme large relative intensities and $\psi < 30^\circ$ diffraction peaks are practically missing. Thus, the **c**-axis orientation of the individual nanocrystals are not perfectly aligned perpendicular to the EES. Moderate intensities of reflection with $30^\circ < \psi < 60^\circ$ values indicate a deviation of about ±15° from the normal of the EES, which indicates an approximately 30–45° scatter of preferred orientation.

## 4. Discussion

Gradually changing mechanical properties of dental enamel arise from the spatial variation of enamel crystal chemistry, prism arrangement and the anisotropy of hydroxyapatite nanocrystals [20,28,37,38]. Location dependent mechanical properties can be well characterized by mapping local hardness (HV) and elastic modulus (E*) using nanoindentation tests. In the present work, it has been shown that HV decreases approximately by 20–30 % from the EES towards to the DEJ in all tested areas (Fig. 4a and b), which is in agreement with the previous studies both on primary [4,24] and permanent teeth [20,34,35] (summary on literature data is tabulated in Appendix E). Studies on permanent enamel have shown 25 % [35], 50 % [20], and 30 % [34] decrease towards DEJ on permanent 3rd molar by indentation technique. Besides these average trends, the non-linear variation of elastic modulus and HV as function of distance from the DEJ was highlighted for young

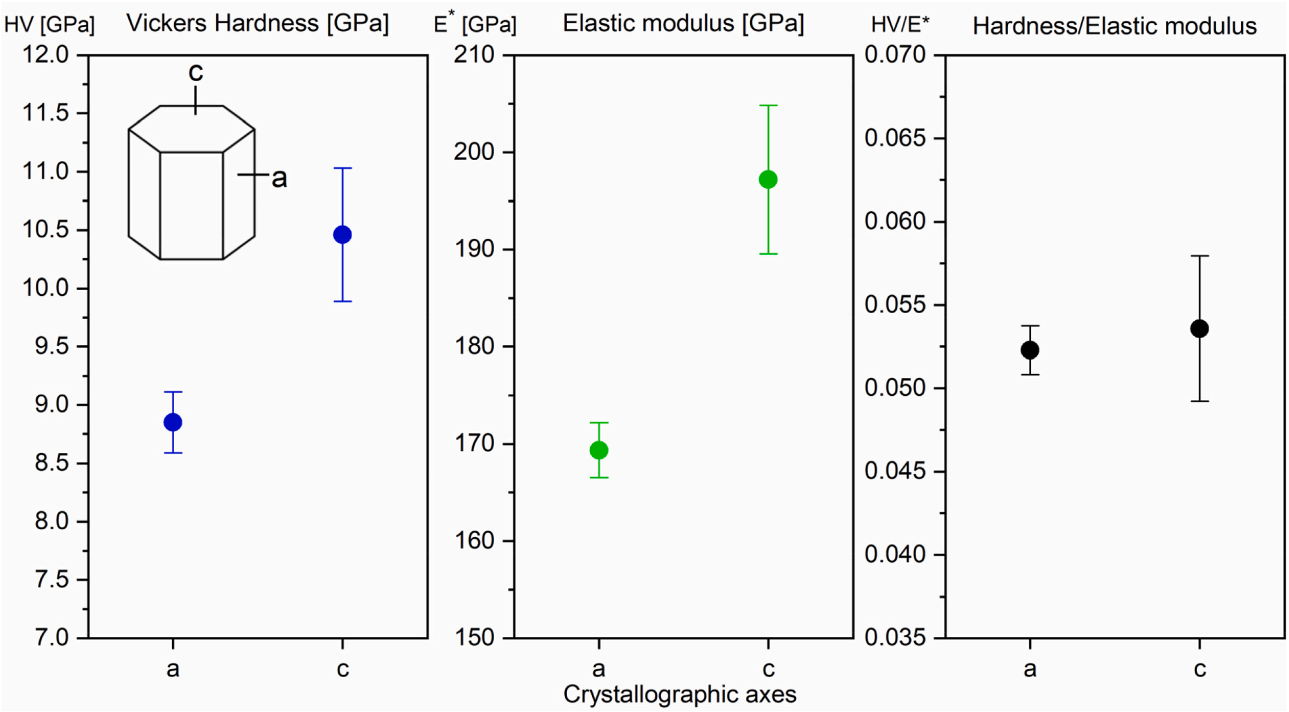

**Fig. 5.** Hardness, elastic modulus and the hardness/elastic modulus ratio obtained on the crystallographic (100) and (001) planes of hydroxyapatite single crystal.

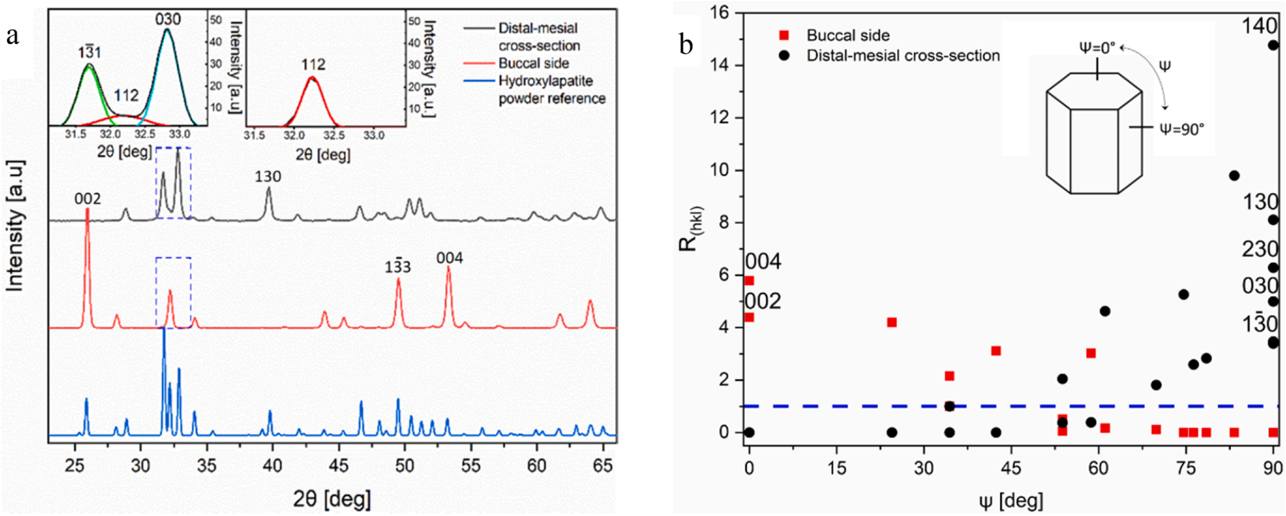

**Fig. 6.** (a) Micro X-ray diffractograms of the distal-mesial cross-section (occlusal side), the buccal surface and the reference random hydroxyapatite powder (crystallite size 0.05 μm). Inserts show the decomposition of the overlapping peaks of the experimental spectra. (b) Texture indices $R_{hkl}$ are plotted as function of the ψ angle between the normal vector of (*hkl*) plane and crystallographic **c** axis. Blue dashed line represents $R_{hkl} = 1$, for randomly oriented hydroxyapatite. Details of the fitting are provided in Appendix B (Fig. B1).

permanent enamel [35], which is similar to our observation on primary enamel (measurement areas 1 and 4). The difference between young and old enamels was attributed to the change of crystal chemistry with time by diffusion processes [35]. Applying nanoindentation mapping for permanent enamel, it has been also shown that HV values, and their change towards the dentin is not uniform in the whole cross section, lingual cusps appear to have higher HV than buccal ones [20]. As for the local variation of HV and elastic modulus along the cross section, the near EES zone of the inter-cuspal regions exhibits the highest hardness [35,37], similarly to our finding on primary tooth (measurement area 5).

Understanding crystallite arrangement and the related structural anisotropy on the length scale commensurate with the nanoindentation measurements is a key issue in the interpretation of mechanical data. Qualitative description of prism microstructure and nanocrystal orientation distribution within prism is based on optical and transmission electron microscopy images [49]. Quantitative assessment of nanocrystal orientation as function of location in enamel cross section is performed by electron [50] and synchrotron diffraction mapping [51,52], however, these studies do not reveal prism microstructure. Recent works focus on the variation of crystallographic parameters [6] and crystal chemistry [53], as function of location with respect to prism microstructure, though only a selected small portion of a whole enamel cross section is studied. Polarization induced contrast (PIC) mapping is able to visualize both crystallite orientation distribution [54] and prism microstructure on the hundreds of micrometre scale [3]. Our SEM image based method provides a simple alternative for the study of prism orientation on a selected cross section over large areas from the DEJ to the enamel external surface. At the same time, allows the extraction of quantitative data on orientation with respect to the image plane, as well, which is the main outcome of the method. This information, together with the crystal structure anisotropy estimated based on micro-XRD, allows a correlation with mechanical data originating from the uppermost few micrometer thick layer of the studied cross section. Furthermore, it allows fast, parametrized comparative studies of microstructure by providing position dependent numerical values to the images. This may be beneficial for the study of demineralisation and remineralisation processes [55,56], enamel affected by pathological hypomineralization [57], and, also for a deeper understanding of evolutionary adaptation [58]. As the applied SEM-based method uses cross sections for prism orientation study, an independent tomography study (e.g. synchrotron) would validate these results, providing a detailed three-dimensional reconstruction of prism orientation [59,60]. However, for a complete description of structural and crystal chemical hierarchies in dental enamel a combination of state-of-the art nanoanalytical techniques is needed [45].

To study separately the contribution of crystal orientation from other factors, first we focus on the crystallographic anisotropy of HV and E*. According to indentation tests performed on hydroxyapatite single crystal, the elastic modulus measured parallel to the [001] axis is approximately 16 % larger than the value obtained in the perpendicular direction, i.e $E_{\mathbf{c}}^*/E_{\mathbf{a}}^* = 1.16$. This anisotropy in the elastic modulus determined using nanoindentation is in good agreement with the anisotropy in the Young's modulus $E_{\mathbf{c}}/E_{\mathbf{a}} = 1.21$ of hydroxyapatite (for details see Appendix C) [61,62]. This anisotropy is associated with the different ability for rotation of $PO_4$ tetrahedra, which is connected to the crystallographic direction dependent motion of both columnar and axial $Ca^{2+}$ ions in the hydroxyapatite structure [63]. Similar relative difference of hardness, $HV_{\mathbf{c}}/HV_{\mathbf{a}} = 1.18$ was measured in the two perpendicular directions. Thus, $E_{\mathbf{c}}^*/E_{\mathbf{a}}^*$ and $HV_{\mathbf{c}}/HV_{\mathbf{a}}$ are expected to be equals, which indicates that HV/E* is practically orientation independent for the hydroxyapatite single crystal. Based on this observation we can anticipate that the spatial variation of the HV/E* in enamel (Fig. 4c) reflects the orientation independent part of the variation of mechanical properties, which is related to a monotonous change of composition from enamel surface toward DEJ, as observed on Fig. 4e and f.

The elastic modulus is primarily a function of the average bond strength of the material, while the hardness also reflects the density of structural defects. Calculation of HV/E* allows to separate these two effects by normalizing the nanohardness with the effect of bond strength [46]. Thus, the variation of HV/E* can be either related to structural defects of individual nanocrystals (e.g. vacancy density due to heterovalent ionic substitution [24] or to the changing volume fraction of protein component between prisms, with substantially different HV/E* ratio [28,64]. According to [20] the variation of HV and E* exhibits the strongest correlation with the average chemistry, namely Ca and P content. Lower levels of Ca and P towards the DEJ correspond to lower degree of mineralization, and related higher ratio of organic material [28]. Separate measurement of the nanomechanical properties of the organic component resulted that its hardness and elastic modulus is 73.6 % and 52.7 % lower than those of the prisms, respectively [29]. This indicates that higher overall ratio of organic material can indeed lead to reduction in HV and, also in HV/E*. Monotonically increasing trends towards the DEJ were published for carbonate-to-phosphate ratio [21] and for Na and Mg concentration [20] as well, this latter is in agreement with our measured data. However, by comparing HV and concentration curves measured in the distal-mesial cross section (Fig. 4), the correlation of composition and mechanical properties is moderate, as the variation of hardness as function of distance from the surface is not monotonous. At the same time HV/E* plots exhibit similar monotonously decreasing tendency from the EES towards the DEJ in measurement areas 1–4 (Fig. 4c). We assume that this can be related to an increasing organic content towards the dentine. A consequence of such variation in organic content is the higher fracture toughness reported close to DEJ [65]. In parallel, minor element concentration also changes monotonously towards the DEJ. Na and Mg increases up to 1.1 at% and 0.6 at%, respectively, while Cl decreases down to 0. It has to be noted that this monotonous trend of Na and Mg concentration is independent from measurement area. All these observations support that the shape of the HV/E* curves correlates better with the change in average crystal chemistry than either the shape of HV or of E* curves.

Crystal orientation was quantified by the variation of XRD peak intensity ratios (Fig. 6). The strong 00*l* reflections on the buccal side and the absence of the same reflections in the distal-mesial cross section indicate that hydroxyapatite nanocrystals exhibit a strong preferred orientation with (001) planes parallel to the EES. As prisms are mostly perpendicular the EES (Fig. 2c), prism elongation direction in average is roughly parallel with crystallographic **c** axis, which is in agreement with most literature data [66,67]. However, beside the strong orientation preference of nanocrystals to the prism axis, variation of the $R_{hkl}$ texture index as function of ψ angle (Fig. 6b) indicates approximately 30-45° of scatter of the orientation. Recent experimental evidences revealed typically 30° but occasionally up to 90° nanocrystal misorientation within each prism, and a more homogeneous orientation distribution (0-30°) of nanocrystals over millimetre sized areas between prisms [3].

Quantitative estimation and separation of the effects of prism orientation and composition variation can be done by analysing the enamel HV and E* data. As the HV/E* proved to be practically orientation independent for hydroxyapatite single crystal, the coefficients $\beta_E = (E^*_{buccal}/E^*_{surface}) - 1$ and $\beta_{HV} = (HV_{buccal}/HV_{surface}) - 1$ for the near EES zone are expected to be equals as well (for calculations see Appendix C). The apparent difference between these ratios ($\beta_E = 0.31$ and $\beta_{HV} = 0.19$ determined from Fig. 4), indicates that HV/E* depends on the local prism orientation, i.e. reflects the mesoscale anisotropy determined by the average crystal orientation under the indenter. Orientation dependent components of E* and HV, $E^*_\varphi$ and $HV_\varphi$, respectively, can be separated from the composition dependent parts, $E^*_0$ and $HV_0$, based on the calculation detailed in the Appendix C. In case of $E^*_\varphi$ and $HV_\varphi$ the composition is kept fixed, while in case of $E^*_0$ and $HV_0$ the orientation is kept fixed. The separation of orientation and composition dependent parts based on experimentally obtained HV and E* data is demonstrated for measurement area 3. Fig. 7a and b show the orientation dependent and composition dependent parts of modulus and hardness, respectively, as a function of position.

Gradual increase in both $E^*_\varphi$ and $HV_\varphi$ towards DEJ is related to the gradual change of prism orientation, which has been determined from SEM image (Fig. 2c). On contrary, an opposite trend is seen for $E^*_0$, and $HV_0$, which accounts for the gradually increasing fraction of organic component toward the DEJ. Orientation dependence of the prisms in the same area was determined using aspect ratio data of SEM images as an independent method (Fig. 2c). Fig. 7c presents the variation of the weighted average of aspect ratio as function of distance from the EES toward DEJ in measurement area 3. The weighting was done using the area of the surface section of the enamel prisms and averaging was done for 50 μm wide stripes parallel to the EES. As prisms have an approximately $A_0 = 1.7$ anisotropy perpendicular to their length due to their characteristic keyhole form cross section, and the aspect ratio is proportional to the cosine of the slope, orientation change of prisms as a function of position can be visualized qualitatively by the difference between the average aspect ratio and $A_0$ as shown in Fig. 7c. Orientation dependence of the prisms can also be determined based on the position dependence of E*(x) and HV(x) as detailed in Appendix D. Fig. 7d shows the spatial change of the prism orientation calculated from E* and HV, from the EES to DEJ. Seemingly, the experimental orientation dependence obtained from SEM imaging shows a fairly good coincidence with the orientation dependence calculated from the hardness and modulus

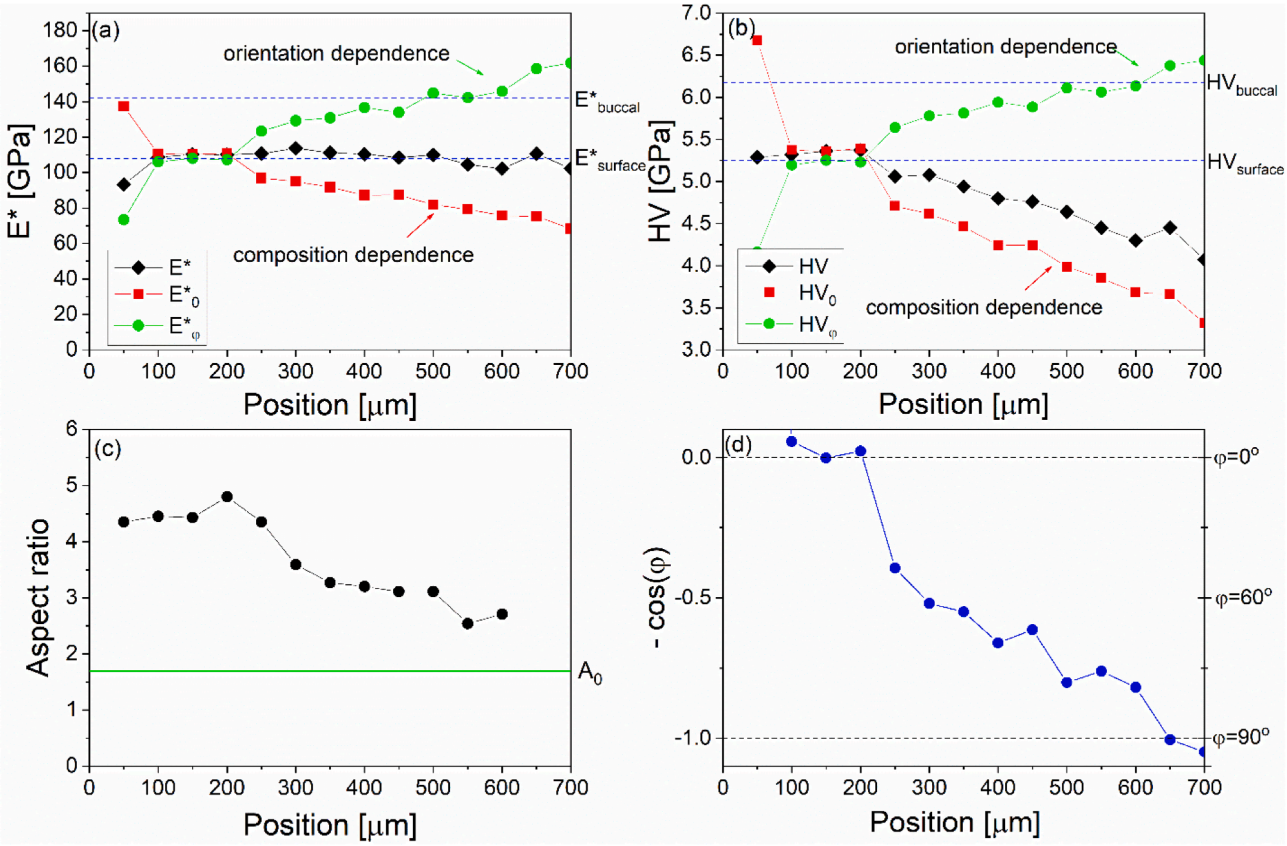

**Fig. 7.** Position dependence of mechanical properties and microstructure of enamel prisms in the distal-mesial cross section of measurement area 3. (a) Experimental elastic modulus (E*) with calculated orientation dependent ($E^*_\varphi$) and composition dependent ($E^*_0$) elastic moduli. (b) Experimental hardness (HV) with calculated orientation dependent ($HV_\varphi$) and composition dependent ($HV_0$) hardness components. (c) Weighted average of prism aspect. $A_0$ at 1.7 indicates the aspect ratio of an enamel prism perpendicular to the elongation axis. (d) Prism orientation as function of position, determined based on experimental elastic modulus and hardness.

(cf. Fig. 7c and d) indicating that mapping of mechanical properties and imaging micromorphological features of dental enamel can be directly related in a quantitative way. At the same time, this coincidence proved to be an independent validation of the correctness of our considerations detailed in Appendix D.

On the diagrams presented on Fig. 7 uniform prism orientation and composition in the 200 μm thick zone near to the EES can be recognized, which is in agreement with SEM and EDS data, respectively. Below this zone both the concentration and orientation dependent components of HV and E* change monotonously, but exhibiting an opposite trend. Increasing $E^*_\varphi$ and $HV_\varphi$ are related to prism orientation variation in the Hunter-Schreger bands. This effect is surpassed by the pronounced effect of composition change, i.e. increasing protein content [28] as indicated by the steep decrease of $HV_0$. This leads to the significant decrease of hardness towards the DEJ, as observed in most experiments. As can be seen in Fig. 7a-b, the method overestimates the effect of prism orientation on hardness and elastic modulus, presumably due to other factors (e.g. concentration dependence of HV/E*) not taken into account so far. However rough estimation and separation of the contribution of crystal chemistry and average prism orientation to the major mechanical parameters have been implemented.

The determined $E^*_\varphi$ and $HV_\varphi$ (Fig. 7a and b) imply the increase of modulus and hardness towards the DEJ in the distal-mesial cross-section due on prism orientation. At the same time, viewing from the buccal direction the opposite trend is expected due to crystal and prism anisotropy. As concentration dependent mechanical parameters are orientation independent, the total modulus of the whole enamel volume exhibits a spectacular elastic anisotropy, developed by the synergistic effect of concentration and orientation gradients. It can be deduced from Fig. 7a, that the modulus shows a negative gradient towards DEJ if measured from the buccal direction because concentration changes monotonically. At the same time, it is nearly constant for the whole enamel volume if measured in cross section due to the combined effect of the composition and orientation (e.g. in the distal mesial section, Fig. 7a E* curve). This anisotropic gradient behaviour ensures the high surface strength of the enamel against strong axial loads (e.g. from the buccal side) and reduces the formation of opening stresses. Hence, due to the minimized vertical gradient of the Young's modulus in any perpendicular direction to the axial load, the possibility of crack formation is reduced as well.

## 5. Conclusion

Mechanical properties of sound primary dental enamel were studied as function of location using nanoindentation mapping, and correlated with chemical composition, nanocrystal and prism orientation, using SEM-EDS, μ-XRD and SEM image processing, respectively. Five areas through the distal-mesial cross-section, and the buccal side of the enamel were characterized in detail. To quantify prism orientation, a novel image processing method was applied, which relies on the uneven secondary electron emission of etched enamel surface. Prism orientation distribution was quantified as function of aspect ratio and inclination angle through the whole cross section. Comparison of the tendencies of major and minor element concentration with variation of Vickers hardness and elastic modulus showed that mechanical properties could not be directly linked to crystal chemistry. At the same time, the spatial variation of nanohardness normalized with elastic modulus exhibited good correlation with changes of average crystal chemistry, namely Ca/P ratio and trace element concentration. Nanoindentation measurements performed on hydroxyapatite single crystal and subsequent theoretical considerations supported that modulus normalized nanohardness is orientation independent and its spatial variation in enamel can be related either to structural defects or changing volume fraction organic material reported in the literature.

Quantitative estimation of the relative contribution of structural anisotropy and crystal chemistry to the mechanical response was provided and orientation dependent and composition dependent components of hardness and elastic modulus were plotted separately as function of location. Composition dependent parts of the hardness and elastic modulus are monotonously decreasing from the external enamel surface towards the DEJ indicating gradual change of average chemistry, which is in agreement with literature data on organic material content, Ca/P ratio and trace element concentrations. Orientation dependent parts of hardness and elastic modulus are monotonously increasing from the external surface towards the DEJ, indicating the change in prism orientation related to variation of average crystal orientation in the Hunter-Schreger bands. Average prism orientation as function of distance from DEJ calculated using experimental hardness and elastic modulus data agrees well with that obtained from geometric parameters obtained from prism orientation maps measured directly on SEM images.

Separation of prism orientation and composition dependent parts of hardness and elastic modulus highlights the elastic anisotropy of the enamel. In addition, it demonstrates that the modulus is nearly constant for the whole enamel volume if measured in cross section, while it exhibits negative gradient towards the DEJ if viewed down the buccal direction. Such spatial variation of modulus guarantees the unique combination of high surface strength and good crack resistance for dental enamel. These findings reveal how two different mechanisms – morphology and crystal chemistry – act simultaneously, creating, and fine tuning the mechanically graded structure of dental enamel. Applying similar controls on microstructure and composition during material synthesis will results improved tuneability of biomimetic composite materials.

## 6. Statement of significance

In this study, we introduced a novel SEM based procedure to obtain quantitative information on prism orientation in primary dental enamel. Prism orientation maps, which represent average crystal orientation on length scales commensurate with the information volume of nanoindentation tests, were compared to mechanical properties and chemical composition at different parts of the enamel. Based on specific assumptions on the mechanical parameters, we separated orientation and composition dependent components of the spatially changing Vickers hardness and elastic moduli and we found that the modulus exhibits the following specific anisotropic gradient behaviour. From the buccal direction, the modulus has a negative gradient towards the dentin enamel junction, while it is nearly constant for the whole enamel volume if measured in cross section. This behaviour results in high surface strength and additionally may be responsible to the superior crack resistance of human enamel.

## Declaration of Competing Interest

The authors declare that they have no known competing financial interests or personal relationships that could have appeared to influence the work reported in this paper.

## Data availability

Data will be made available on request.

## Acknowledgements

We are grateful to Mr. Csanád Lóránth for providing the hydroxyapatite single crystal mineral sample. This work was supported by the National Research, Development and Innovation Fund Office, Hungary under the Project "Investigation of the nanostructural background of functionality in case of biogenic and biocompatible mineral apatite", grant number K-125100.

## Appendix A. Supplementary data

Supplementary data to this article can be found online at https://doi.org/10.1016/j.matdes.2023.112369.

## References

[1] M.J. Buehler, Tu(r)ning weakness to strength, Nano Today 5 (2010) 379–383, https://doi.org/10.1016/j.nantod.2010.08.001.

[2] J. Wilmers, S. Bargmann, Nature's design solutions in dental enamel: Uniting high strength and extreme damage resistance, Acta Biomater. 107 (2020) 1–24, https://doi.org/10.1016/j.actbio.2020.02.019.

[3] E. Beniash, C.A. Stifler, Ch-Y. Sun, G.S. Jung, M.J. Buehler, P.U.P.A. Gilbert, The hidden structure of human enamel, Nat. Commun. 10 (2019) 4383 https://doi.org/, doi: 10.1038/s41467- 019- 12185- 7.

[4] I.M. Low, N. Duraman, U. Mahmood, Mapping the structure, composition and mechanical properties of human teeth, Mater. Sci. Eng. C 28 (2008) 243–247, https://doi.org/10.1016/j.msec.2006.12.013.

[5] A.R. Studard, Biological and bioinspired composites with spatially tunable heterogeneous architectures, Adv. Funct. Mater. 23 (2013) 4423–4436, https://doi.org/10.1002/adfm.201300340.

[6] R. Free, K. DeRocher, V. Cooley, R. Xu, S.R. Stock, D. Joester, Mesoscale structural gradients in human tooth enamel, PNAS 119 (2022), https://doi.org/10.1073/pnas.2211285119.

[7] G. Daculsi, B. Kerebel, High-resolution electron microscope study of human enamel crystallites: Size, shape, and growth, J. Ultrastruct. Res. 65 (1978) 163–172, https://doi.org/10.1016/S0022-5320(78)90053-9.

[8] G. Daculsi, J. Menanteau, L.M. Kerebel, D. Mitre, Length and shape of enamel crystals, Calcif. Tissue Int. 36 (1984) 550–555, https://doi.org/10.1007/BF02405364.

[9] F.Z. Cui, J. Ge, New observations of the hierarchical structure of human enamel, from nanoscale to microscale, JTERM 1 (3) (2007) 185–191, https://doi.org/10.1002/term.21.

[10] A. Nanci, Ten Cate's Oral Histology, ninth ed., Elsevier, 2018.

[11] A. Boyde, The development of enamel structure, Proc. R. Soc. Med. 60 (1967) 923–928. PMID: 6055492.

[12] S.N. White, W. Luo, M.L. Paine, H. Fong, M. Sarikaya, M.L. Snead, Biological organization of hydroxyapatite crystallites into a fibrous continuum toughens and controls anisotropy in human enamel, J. Dent. Res. 80 (2001) 321–326, https://doi.org/10.1177/00220345010800010501.

[13] D. Zaytsev, P. Panfilov, Anisotropy of the mechanical properties of human dental enamel, Mater. Lett. 159 (2015) 428–431, https://doi.org/10.1016/j.matlet.2015.07.057.

[14] B. An, R. Wang, D. Zhang, Role of crystal arrangement on the mechanical performance of enamel, Acta Biomater. 8 (2012) 3784–3793, https://doi.org/10.1016/j.actbio.2012.06.026.

[15] J.C. Elliott, Calcium phosphate biominerals, Rev. Mineral. Geochem. 48 (2002) 427–453, https://doi.org/10.2138/rmg.2002.48.11.

[16] H. C. W. Skinner, H. Ehrlich, Biomineralization, in: Treatise on Geochemistry: Second Edition, Elsevier Inc. 10, 2013, pp. 105–162. doi.org/10.1016/B978-0-08-095975-7.00804-4.

[17] C. Robinson, J.A. Weatherell, A.S. Hallsworth, Distribution of magnesium in mature human enamel, Caries Res. 15 (1981) 70–77, https://doi.org/10.1159/000260502.

[18] R.Z. Le Geros, T. Sakae, C. Bautista, M. Retino, J.P. Le Geros, Magnesium and carbonate in enamel and synthetic apatites, Adv. Dent. Res. 10 (1996) 225, https://doi.org/10.1177/0895937496010 0 021801.

[19] E. Wentrup-Byrne, C.A. Armstrong, R.S. Armstrong B.M. Collins, Fourier transform Raman microscopic mapping of the molecular components in a human tooth, J. of Raman Spectroscopy, 28 (1997) 151–158. doi:10.1002/(sici)1097-4555(199702)28:2/3<151::aid-jrs71>3.0.co;2-5.

[20] J.L. Cuy, A.B. Mann, K.J. Livi, M.F. Teaford, T.P. Weihs, Nanoindentation mapping of the mechanical properties of human molar tooth enamel, Arch. Oral Biol. 47 (2002) 281–291, https://doi.org/10.1016/s0003-9969(02)00006-7.

[21] C. Xu, R. Reed, J.P. Gorski, Y. Wang, M.P. Walker, The distribution of carbonate in enamel and its correlation with structure and mechanical properties, J. of Mat. Sci. 47 (23) (2012) 8035–8043.

[22] K.A. DeRocher, P.J.M. Smeets, B.H. Goodge, M.J. Zachman, P.V. Balachandran, L. Stegbauer, M.J. Cohen, L.M. Gordon, J.M. Rondinelli, L.F. Kourkoutis, D. Joester, Chemical gradients in human enamel crystallites, Nature 583 (2020) 66–71, https://doi.org/10.1038/s41586-020-2433-3.

[23] M.N. Abdallah, H. Eimar, D.C. Bassett, M. Schnabel, O. Ciobanu, V. Nelea, M. D. McKee, M. Cerruti, F. Tamimi, Diagenesis-inspired reaction of magnesium ions with surface enamel mineral modifies properties of human teeth, Acta Biomater. 37 (2016) 174–183, https://doi.org/10.1016/j.actbio.2016.04.005.

[24] V.K. Kis, A. Sulyok, M. Hegedűs, I. Kovács, N. Rózsa, Z. Kovács, Magnesium incorporation into primary dental enamel and its effect on mechanical properties, Acta Biomater. 120 (2021) 104–115, https://doi.org/10.1016/j.actbio.2020.08.035.

[25] Y.-L. Wang, H.-H. Chang, Y.-C. Chiang, C.-H. Lin, C.-P. Lin, Strontium ion can significantly decrease enamel demineralization and prevent the enamel surface hardness loss in acidic environment, J. Formos. Med. Assoc. 118 (2019) 39–49, https://doi.org/10.1016/j.jfma.2018.01.001.

[26] E.D. Yilmaz, J. Koldehoff, G.A. Schneider, On the systematic documentation of the structural characteristics of bovine enamel: A critic to the protein sheath concept, Dent. Mater. 34 (2018) 1518–1530, https://doi.org/10.1016/j.dental.2018.06.006.

[27] R.P. Shellis, G.H. Dibdin, Enamel microporosity and its functional implications, in: M.F. Teaford, M. Meredith Smith, M.W.J. Ferguson (Eds.), Development, Function and Evolution of Teeth, Cambridge University Press, 2000, pp. 242–251.

[28] L.H. He, M.V. Swain, Understanding the mechanical behaviour of human enamel from its structural and compositional characteristics, J. Mechan Behavior Biomed. Mater. 1 (2008) 18–29, https://doi.org/10.1016/j.jmbbm.2007.05.001.

[29] J. Ge, F.Z. Cui, X.M. Wang, H.L. Feng, Property variations in the prism and the organic sheath within enamel by nanoindentation, Biomaterials 26 (2005) 3333–3339, https://doi.org/10.1016/j.biomaterials.2004.07.059.

[30] S.F. Ang, M. Saadatmand, M.V. Swain, A. Klocke, G.A. Schneider, Comparison of mechanical behaviors of enamel rod and interrod regions in enamel, J. Mater. Res. 27 (2012) 448–456, https://doi.org/10.1557/jmr.2011.409.

[31] M. Shahmoradi, L.E. Bertassoni, H.M. Elfallah, M. Swain, Fundamental Structure and Properties of Enamel, Dentin and Cementum, in: Advances in Calcium Phosphate Biomaterials, Springer Inc., 2014, pp. 511-547. doi.org/10.1007/978-3-642-53980-0_17.

[32] H.H.K. Xu, D.T. Smith, S. Jahanmir, E. Romberg, J.R. Kelly, V.P. Thompson, E. D. Rekow, Indentation damage and mechanical properties of human enamel and dentin, J. Dent. Res. 77 (1998) 472–480, https://doi.org/10.1177/00220345980770030601.

[33] S. Habelitz, S.J. Marshall, G.W. Marshall, M. Balooch, Mechanical properties of human dental enamel on the nanometre scale, Arc. Oral Biol. 46 (2) (2001) 173–183.

[34] S. Roy, B. Basu, Mechanical and tribological characterization of human tooth, Mater Charact 59 (2008) 747–756, https://doi.org/10.1016/j.matchar.2007.06.008.

[35] S. Park, J.B. Quinn, E. Romberg, D. Arola, On the brittleness of enamel and selected dental materials, Dent. Mater. 24 (2008) 1477–1485, https://doi.org/10.1016/j.dental.2008.03.007.

[36] Y.-R. Zhang, W. Du, X.-D. Zhou, H.-Y. Yu, Review of research on the mechanical properties of the human tooth, Int. J. Oral Sci. 6 (2014) 61–69, https://doi.org/10.1038/ijos.2014.21.

[37] L. Shen, F. Barbosa de Sousa, N. Tay, T.S. Lang, V.L. Kaixin, J. Han, L. Kilpatrick-Liverman, W. Wang, S. Lavender, S. Pilch, H.Y. Gan, Deformation behavior of normal human enamel: A study by nanoindentation, J. Mech. Behav. Biomed. Mater. 108 (2020), 103799, https://doi.org/10.1016/j.jmbbm.2020.103799.

[38] T. Sui, M.A. Sandholzer, N. Baimpas, I.P. Dolbnya, G. Landini, A.M. Korsunsky, Hierarchical modelling of elastic behaviour of human enamel based on synchrotron diffraction characterization, J. Struct. Biol. 184 (2013) 136–146, https://doi.org/10.1016/j.jsb.2013.09.023.

[39] A. Braly, L.A. Darnell, A.B. Mann, M.F. Teaford, T.P. Weihs, The effect of prism orientation on the indentation testing of human molar enamel, Arch. Oral Biol. 52 (9) (2007) 856–860, https://doi.org/10.1016/j.archoralbio.2007.03.005.

[40] I.M. Low, Depth-profiling of crystal structure, texture, and microhardness in a functionally graded tooth enamel, J. Am. Ceram. Soc. 87 (2004) 2125–2131, https://doi.org/10.1111/j.1151-2916.2004.tb06369.x.

[41] W.C. Oliver, G.M. Pharr, An improved technique for determining hardness and Elastic modulus using load and displacement sensing indentation experiments, J. Mater. Res. 7 (6) (1992) 1564–1583, https://doi.org/10.1557/JMR.1992.1564.

[42] W.H. Arnold, B. Haddad, K. Schaper, K. Hagemann, C. Lippold, G. Danesh, Enamel surface alterations after repeated conditioning with HCl, Head Face Med. 11 (2015) 32, https://doi.org/10.1186/s13005-015-0089-2.

[43] C.A. Schneider, W.S. Rasband, K.W. Eliceiri, NIH Image to ImageJ: 25 years of image analysis, Nat. Methods 9 (2012) 671–675.

[44] D.K. Whittaker, D. Richards, Scanning electron microscopy of the neonatal line in human enamel, Arch. Oral Biol. 23 (1978) 45–50, https://doi.org/10.1016/0003-9969(78)90052-3.

[45] C. Besnard, A. Marie, S. Sasidharan, R.A. Harper, R.M. Shelton, G. Landini, A. M. Korsunsky, Synchrotron X-ray studies of the structural and functional hierarchies in mineralised human dental enamel: A state-of-the-art review, Dentistry J. 11 (2023) 98, https://doi.org/10.3390/dj11040098.

[46] Z.S. Kovács, M. Fábián, N. Szász, I. Székács, V.K. Kis, Tracking the initial stage of bioactive layer formation on Si-Ca-Na-P oxide glasses by nanoindentation, J. Non Cryst. Solids 581 (2022), 121416.

[47] W.E.G. Müller, M. Ackermann, M. Neufurth, E. Tolba, S. Wang, Q. Feng, H. C. Schröder, X. Wang, A novel biomimetic approach to repair enamel cracks/carious damages and to reseal dentinal tubules by amorphous polyphosphate, Polymers 9 (2017) 120, https://doi.org/10.3390/polym9040120.

[48] S. Saber-Samandari, K.A. Gross, Micromechanical properties of single crystal hydroxyapatite by nanoindentation, Acta Biomater. 56 (2009) 2206–2212, https://doi.org/10.1016/j.actbio.2009.02.009.

[49] A.H. Meckel, W.J. Griebstein, R.J. Neal, Structure of mature human dental enamel as observed by electron microscopy, Arch. Oral Biol. 10, 5 (1965) 775–783, https://doi.org/10.1016/0003-9969(65)90131-7.

[50] A. Koblischka-Veneva, M.R. Koblischka, J. Smauch, M. Hannig, Human dental enamel: A natural nanotechnology masterpiece investigated by TEM and t-EBSD, Nano Res. 11 (2018) 3911–3921, https://doi.org/10.1007/s12274-018-1968-1.

[51] M. Al-Jawad, A. Steuwer, S.H. Kilcoyne, R.C. Shore, R. Cywinski, D.J. Wood, 2D mapping of texture and lattice parameters of dental enamel, Biomaterials 28 (18) (2007) 2908–2914, https://doi.org/10.1016/j.biomaterials.2007.02.019.

[52] M. Al-Mosawi, G.R. Davis, A. Bushby, J. Montgomery, J. Beaumont, M. Al-Jawad, Crysallographic texture and mineral concentration quantification of developing and mature human incisal enamel, Sci. Rep. 8 (2018) 14449, https://doi.org/10.1038/s41598-018-32425-y.

[53] C. Besnard, A. Marie, S. Sasidharan, P. Bucek, J.M. Walker, J.E. Parker, T.E. J. Moxham, B. Daurer, B. Kaulich, M. Kazemian, R.M. Shelton, G. Landini, A. M. Korsunky, Nanoscale correlative X-ray spectroscopy and ptychography of carious dental enamel, Mater. Des. 224 (2022), 111272, https://doi.org/10.1016/j.matdes.2022.111272.

[54] B. Hesse, D. Stier, M. Cotte, J.-B. Forien, P. Zaslansky, Polarization induced contrast X-ray fluorescence at submicrometer resolution reveals nanometer apatite crystal orientations across entire tooth sections, Biomed. Opt. Express 10 (1) (2019) 18–28, https://doi.org/10.1364/BOE.10.000018.

[55] T. Sui, E. Salvati, R.A. Harper, H. Zhang, R.M. Shelton, G. Landini, A.M. Korsunsky, In situ monitoring and analysis of enamel demineralisation using synchrotron X-ray scattering, Acta Biomater. 77 (2018) 333–341, https://doi.org/10.1016/j.actbio.2018.07.027.

[56] A. Hou, J. Luo, M. Zhang, J. Li, W. Chu, K. Liang, J. Yang, J. Li, Two-in-one strategy: a remineralizing and anti-adhesive coating against demineralized enamel, International, J. Oral Sci. 12 (2020), https://doi.org/10.1038/s41368-020-00097-y.

[57] K. Elhennawy, K. Bekes, A. Dobsak, S. Tangl, H. Shokoohi-Tabrizi, F. Schwendicke, Structural, mechanical, and chemical evaluation of molar incisor hypomineralization-affected enamel, in: K. Bekes (Ed.), Molar Incisor Hypomineralization: A Clinical Guide to Diagnosis and Treatment, Springer International Publishing, Cham, 2020, pp. 11–20.

[58] G.T. Schwartz, A. McGrosky, D.S. Strait, Fracture mechanics, enamel thickness and the evolution of molar form inhominins, Biol. Lett. 16 (2020), https://doi.org/10.1098/rsbl.2019.0671.

[59] S.E.P. Dowker, J.C. Elliott, G.R. Davis, R.M. Wilson, P.C. Cloetens, Synchrotron X-ray microtomographic investigation of mineral concentrations at micrometre scale in sound and carious enamel, Caries Res. 38 (2004) 514–522, https://doi.org/10.1159/000080580.

[60] C. Besnard, A. Marie, P. Bucek, S. Sasidharan, R.A. Harper, S. Marathe, K. Wanelik, G. Landini, R.M. Shelton, A.M. Korsunsky, Hierarchical 2D to 3D micro/nano-histology of human dental caries lesions using light, X-ray and electron microscopy, Mater. Des. 220 (2022), 110829, https://doi.org/10.1016/j.matdes.2022.110829.

[61] F. Brunet, D.R. Allan, S.A.T. Redfern, R.J. Angel, R. Miletich, H.J. Reichmann, J. Sergent, M. Hanfland, Compressibility and thermal expansivity of synthetic apatites, $Ca_5(PO_4)_3X$ with $X = OH$, F and Cl, Eur. J. Mineral. 11 (6) (1999) 1023–1036.

[62] W. Sailuam, K. Phacheerak, A. Bootchanont, I. Fongkaew, S. Limpijumnong, Elastic and mechanical properties of hydroxyapatite under pressure: A first-principles investigation, Comput. Condens. Matter 24 (2020) e00481.

[63] A. Zamiri, S. De, Mechanical properties of hydroxyapatite single crystals from nanoindentation data, J. Mech. Behav. Biomed. Mater. 4 (2011) 146–152, https://doi.org/10.1016/j.jmbbm.2010.11.001.

[64] Z.-H. Xie, M.V. Swain, G. Swadener, P. Munroe, M. Hoffman, Effect of microstructure upon elastic behaviour of human tooth enamel, J. Biomech. 42 (2009) 1075–1080, https://doi.org/10.1016/j.jbiomech.2009.02.004.

[65] Q. Zheng, H. Xu, F. Song, L. Zhang, X. Zhou, Y. Shao, D. Huang, Spatial distribution of the human enamel fracture toughness with aging, J. Mech. Behav. Biomed. Mater. 26 (2013) 148–154.

[66] L.M. Simmons, M. Al-Jawad, S.H. Kilcoyne, D.J. Wood, Distribution of enamel crystallite orientation through an entire tooth crown studied using synchrotron X-ray diffraction, Eur. J. Oral Sci. 119 (2011) 19–24, https://doi.org/10.1111/j.1600-0722.2011.00909.x.

[67] L. Raue, H. Klein, Location depending textures of the human dental enamel, Solid State Phenom. 160 (2010) 281–286, https://doi.org/10.4028/www.scientific.net/SSP.160.281.